Experimental Study of Turbulent Fluctuations in Hydraulic Jumps

Hang Wang[1] and Hubert Chanson[2]

Abstract: In an open channel, the transformation from a supercritical flow into a subcritical flow is a rapidly varied flow with large turbulent fluctuations, intense air entrainment, and substantial energy dissipation called a hydraulic jump. New experiments were conducted to quantify its fluctuating characteristics in terms of free-surface and two-phase flow properties for a wide range of Froude numbers ($3.8 < F_1 < 8.5$) at relatively large Reynolds numbers ($2.1 \times 10^4 < R < 1.6 \times 10^5$). The time-averaged free-surface profile presented a self-similar profile. The longitudinal movements of the jump were observed, showing both fast and very slow fluctuations for all Froude numbers. The air–water flow measurements quantified the intense aeration of the roller. Overall the present findings demonstrated the strong interactions between the jump roller turbulence and free-surface fluctuations. **DOI: 10.1061/(ASCE)HY.1943-7900.0001010.**

Author keywords: Hydraulic jumps; Turbulent fluctuations; Free-surface profile; Air–water flows; Physical modeling; Jump toe oscillations.

Introduction

In an open channel, the transformation from a supercritical flow into a subcritical flow is called a hydraulic jump. The transition is a rapidly varied flow with large turbulent fluctuations, intense air entrainment, and substantial energy dissipation. For a hydraulic jump in a smooth horizontal prismatic channel, the continuity and momentum principles yield a relationship between the upstream and downstream flow depths, d_1 and d_2, respectively, and the energy principle gives an expression of the total head loss ΔH in the jump

$$\frac{d_2}{d_1} = \frac{1}{2} \times \left(\sqrt{1 + 8 \times F_1^2} - 1 \right) \quad (1)$$

$$\frac{\Delta H}{d_1} = \frac{1}{16} \times \frac{(\sqrt{1 + 8 \times F_1^2} - 3)^3}{\sqrt{1 + 8 \times F_1^2} - 1} \quad (2)$$

where F_1 = upstream Froude number, $F_1 = V_1/(g \times d_1)^{1/2}$; V_1 = upstream velocity; and g = gravity acceleration (Henderson 1966; Liggett 1994; Chanson 2012). When the inflow Froude number is slightly larger than unity, the hydraulic jump is characterized by a relative smooth and continuous rise in water depth, followed by free-surface undulations, an undular jump. An undular jump develops into a breaking jump when the inflow Froude number is greater than a critical value, which depends upon the development of inflow boundary layer at the channel bed (Chanson and Montes 1995; Ohtsu et al. 2001). For inflow Froude numbers greater than 3 or 4, the hydraulic jump is characterized by a breaking roller with surface splashing, air entrainment, and large scale turbulence development (Rajaratnam 1967; Hager 1992; Chanson 2009). The jump toe is a singular point in the free-surface profile, and the turbulent two-phase flow region immediately downstream the jump toe is called the jump roller. The flow features in the jump roller are extremely complicated because of the turbulent nature of the roller motion (Resch et al. 1974; Babb and Aus 1981; Lennon and Hill 2006). For the last 30 years, a number of physical studies specifically investigated the turbulent flow field in hydraulic jumps (Table 1). To date, the knowledge into the roller free-surface fluctuations and turbulent air–water flow remains limited.

The present study examines in detail the fluctuations of the roller surface together with the two-phase flow properties. The study is based upon some experimental results conducted in a relatively large facility covering for a wide range of Froude numbers ($3.8 < F_1 < 8.5$) at relatively large Reynolds numbers ($2.1 \times 10^4 < R < 1.6 \times 10^5$). It is the aim of this work to characterize the fluctuating properties of hydraulic jumps with breaking roller and provide new insights into the interactions between roller turbulence and free-surface fluctuations.

Experimental Facility and Instrumentation

New experiments were conducted in a horizontal rectangular flume at the University of Queensland (Brisbane, Australia). The 3.2 m long 0.5 m wide test section was made of smooth high-density polyethylene (HDPE) bed and glass sidewalls (Fig. 1). The water was supplied by a constant head tank feeding a large intake structure leading to the test section through a vertical rounded gate. The sluice had a semicircular rounding ($Ø = 0.3$ m), inducing a horizontal inflow at the inlet. Flow straighteners and meshes were installed in the intake structure to provide a smooth approach flow upstream of the rounded gate. The tailwater conditions were controlled by a vertical overshoot gate located at $x = 3.2$ m, where x is the longitudinal distance from the test section's upstream end.

The discharge was measured with a Venturi meter calibrated on site. The clear-water flow depths were measured with point gauges

[1]Research Student, School of Civil Engineering, Univ. of Queensland, Brisbane, QLD 4072, Australia.

[2]Professor in Hydraulic Engineering, School of Civil Engineering, Univ. of Queensland, Brisbane, QLD 4072, Australia (corresponding author). E-mail: h.chanson@uq.edu.au

Note. This manuscript was submitted on May 14, 2014; approved on January 19, 2015; published online on March 3, 2015. Discussion period open until August 3, 2015; separate discussions must be submitted for individual papers. This paper is part of the ***Journal of Hydraulic Engineering***, © ASCE, ISSN 0733-9429/04015010(10)/$25.00.

Table 1. Experimental Investigations of Turbulent Fluctuations in Hydraulic Jumps

Reference	W (m)	x_1 (m)	d_1 (m)	F_1	R	Instrumentation
Resch et al. (1974)	0.39	0.39–7.8	0.012 and 0.039	3.0–8.0	2.4×10^4–9.7×10^4	Hot-film probe (Ø = 0.6 mm)
Babb and Aus (1981)	0.465	—	0.035	6.0	1.2×10^5	Hot-film probe (Ø = 0.4 mm)
Long et al. (1991)	0.47	0.04–0.08	0.025	4–9	4.9×10^4–1.1×10^5	High-speed video camera
Liu et al. (2004)	0.46	<0.1	0.041–0.071	2.0–3.3	8.6×10^4–1.5×10^5	Acoustic Doppler velocimeter (ADV) with down-looking head
Lennon and Hill (2006)	0.30	—	0.02–0.031	1.4–3.0	7.9×10^4–9.1×10^4	Particle image velocimetry (PIV)
Vallé and Pasternack (2006)	2[a]	—	0.22	2.8	9×10^5	Time domain reflectometry (TDR)
Chanson (2007)	0.25 and 0.50	0.50 and 1.00	0.013–0.029	5.1–8.6	2.5×10^4–9.8×10^4	Array of single-tip phase detection probes (Ø = 0.35 mm)
Murzyn et al. (2007)	0.3	0.18–0.43	0.021–0.059	1.9–4.8	3.2×10^4–8.9×10^4	Wire gauges and high-speed video camera
Chanson (2011a)	0.50	0.75	0.018–0.019	3.58–12.43	2.9×10^4–9.3×10^4	Visual observations
	0.50	0.75	0.018	5.14–11.2	4.0×10^4–8.3×10^4	Dual-tip phase detection probe (Ø = 0.25 mm)
Present study	0.50	0.80–1.87	0.012–0.047	3.8–8.5	2.1×10^4–1.6×10^5	Acoustic displacement meters, video cameras, dSLR cameras and dual-tip phase detection probe (diameter = 0.25 mm)

[a]Field investigation.

with an accuracy of 0.2 mm. In the clear water flow region, the velocity was measured with a Prandtl-Pitot tube (Ø = 3.0 mm). The fluctuating free-surface elevations above the hydraulic jump were recorded nonintrusively by using acoustic displacement meters Microsonic Mic+25/IU/TC (Microsonic, Germany) and Mic+35/IU/TC. A total of 15 displacement meters were mounted above the channel [Fig. 1(a)], enabling simultaneous and nonintrusive measurements of instantaneous water surface locations. The signals were sampled at 50 Hz for at least 540 s to record both low-frequency and high-frequency free-surface fluctuations. The air–water flow properties were measured with a dual-tip conductivity probe ($\Delta x = 7.46$ mm, $\Delta z = 1.75$ mm) equipped with two identical needle sensors with an inner diameter of 0.25 mm. The phase detection probe was excited by an electronic system (Ref. UQ82.518) and the signal outputs were sampled at 20 kHz per sensor for 45 s. The elevation of the probe was supervised by a Mitutoyo digimatic scale unit with a vertical accuracy less than 0.05 mm. Movies and photographs were taken with a Sony HD digital video camera and Pentax dSLR camera, respectively.

Experimental Flow Conditions

Detailed measurements were conducted for $3.8 < F_1 < 8.5$, using an upstream flow depth $d_1 = 0.02$ m. Further experiments were performed with $F_1 = 5.1$ for 0.012 m $< d_1 <$ 0.047 m corresponding to $2 \times 10^4 < R < 1.6 \times 10^5$, where $R = \rho \times V_1 \times d_1/\mu$; ρ is the water density; and μ is the water dynamic viscosity. The experimental flow conditions are summarized in Table 2, where Q is the water discharge; x_1 is the distance between the jump toe and the upstream vertical gate; and h is the upstream undershoot gate opening. Resch et al. (1974) showed differences between hydraulic jumps with undeveloped and fully developed inflow. In this paper, the inflow was characterized by a partially developed boundary layer ($\delta/d_1 < 1$), and the jump toe position was allowed to shift freely back and forth about its mean location.

A 3×4 array of displacement meters was positioned over the jump. Three more sensors were placed horizontally above the inflow free-surface to record the roller's longitudinal position [Fig. 1(a)]. The axes of horizontal sensors were approximately 25 mm above the water surface. The dual-tip probe was located on the channel centerline. Further details were presented in Wang and Chanson (2013).

Free-Surface Characteristics

Upstream of the jump toe, all visual, photographic, and video observations indicated that the free-surface was flat and quasi-horizontal. The impingement point was characterized by a marked discontinuity of the free-surface slope at $x = x_1$ (on average). The observations showed a sharp rise in water level in the downstream direction above the turbulent jump roller, i.e., $x > x_1$ [Fig. 1(a)]. The time-averaged free-surface profiles of the roller were measured with the acoustic displacement meters, and the data were supplemented with point gauge measurements. The ratio of conjugate depths d_2/d_1 presented a good agreement with the momentum principle [Eq. (1)]. The roller free-surface profiles were observed to present a self-similar profile. The experimental data are shown in Fig. 2 together with the self-similar function

$$\frac{\eta - d_1}{d_2 - d_1} = \left(\frac{x - x_1}{L_r}\right)^{0.54} \tag{3}$$

where η = (time-averaged) free-surface elevation above the invert; x_1 = jump toe location; and L_r = roller length defined as the

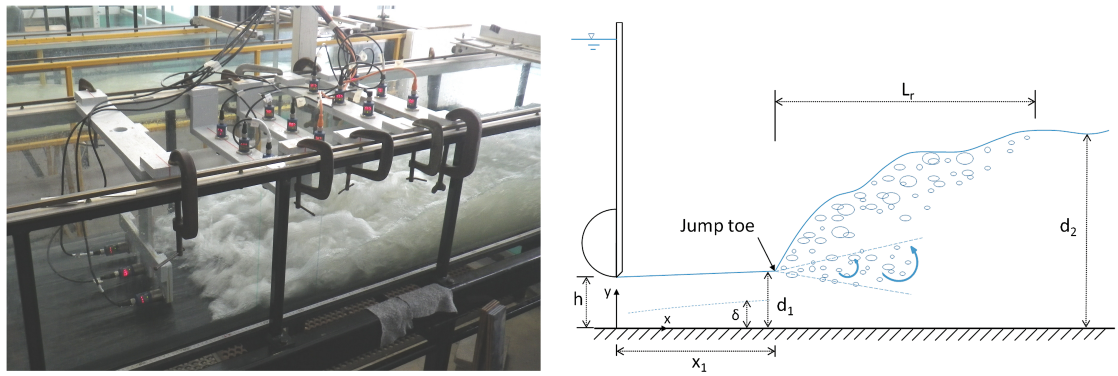

Fig. 1. Experimental facility and definition sketch: (a) flow conditions: $Q = 0.0368$ m^3/s, $d_1 = 0.0277$ m, $x_1 = 1.083$ m, $F_1 = 5.1$, $R = 7.4 \times 10^4$, and flow direction from left to right; (b) definition sketch of hydraulic jump flow structure in experimental channel

distance from the jump toe over which the mean free-surface level increased monotically [Fig. 1(b)]. The experimental results are compared with previous experimental data, Eq. (3), and the profiles proposed by Valiani (1997) and Chanson (2011b) in Fig. 2.

The dimensionless roller length L_r/d_1 was observed to increase with increasing inflow Froude number. The data were compared with previous observations using similar instrumentation and with the empirical correlations of Murzyn et al. (2007) [Fig. 3(a)]. For all the data shown in Fig. 3(a), L_r/d_1 tended to follow a linear trend

$$\frac{L_r}{d_1} = 6 \times (F_1 - 1) \quad 1.5 < F_1 < 8.5 \tag{4}$$

Eq. (4) is compared with experimental data in Fig. 3(a). The values of d_2 and L_r are reported in a tabular format in Table 2. The jump roller was also visually identified as the flow region with increasing water depth and significant free-surface spray and splashing. The visual observations are compared with the (aforementioned) data extracted from the free-surface profile measurements in Fig. 3(b). The comparison suggested that the visual observations underestimated the measured roller length by approximately 20% [Fig. 3(b)]. The differences were linked to the visual estimate of the roller's downstream end, because any visual observation involved subjective judgement and uncertainties.

Jump Toe Fluctuations

For all investigated flow conditions, the hydraulic jump toe shifted about a mean position $x = x_1$ in both fast and slow manners. Both types of fluctuating motion were investigated in this paper. Some experiments were run for relatively long periods between, 27 and 160 min; and both the longitudinal position of roller toe and surface elevations were recorded. The observations highlighted some temporary changes of jump toe position ranging from $-14 \times d_1$ to $+6 \times d_1$. The roller tended to stay at some remote positions for approximately 120–400 s before returning to its mean position. The horizontal displacement range was larger than for the rapid jump toe oscillations, and the associated periods were drastically longer. A typical data set in terms of the relative jump toe position $x - x_1$ is presented in Fig. 4. The data set illustrates that some major movements were linked to some upstream migration ($x - x_1 < 0$) (Fig. 4). More than 20% of the instantaneous jump toe positions were recorded at the mean position ($x - x_1 = 0$). The probability density function was skewed toward the upstream side ($x - x_1 < 0$), and the cumulative percentages on the two sides were comparable (37.5% upstream and 42.2% downstream). For the data shown in Fig. 4, approximately 36 major shifts in jump position were recorded within the 160-min record corresponding to an average

Table 2. Experimental Flow Conditions of the Present Study

Q (m^3/s)	H (m)	x_1 (m)	d_1 (m)	F_1	R	d_2 (m)	L_r (m)
0.0160	0.012	0.50	0.012	5.1	2.1×10^4	—	—
0.0179	0.020	0.83	0.0206	3.8	3.5×10^4	0.095	0.28
0.0239	0.020	0.83	0.0209	5.1	4.8×10^4	0.139	0.52
0.0356	0.020	0.83	0.0206	7.5	6.8×10^4	0.202	0.80
0.0397	0.020	0.83	0.0208	8.5	8.0×10^4	0.234	1.0
0.0368	0.026	1.08	0.0277	5.1	7.4×10^4	—	—
0.0463	0.030	1.25	0.0322	5.1	9.2×10^4	0.209	0.85
0.0552	0.034	1.42	0.0363	5.1	1.10×10^5	—	—
0.0689	0.040	1.67	0.042	5.1	1.37×10^5	—	—
0.0815	0.045	1.87	0.047	5.1	1.63×10^5	—	—

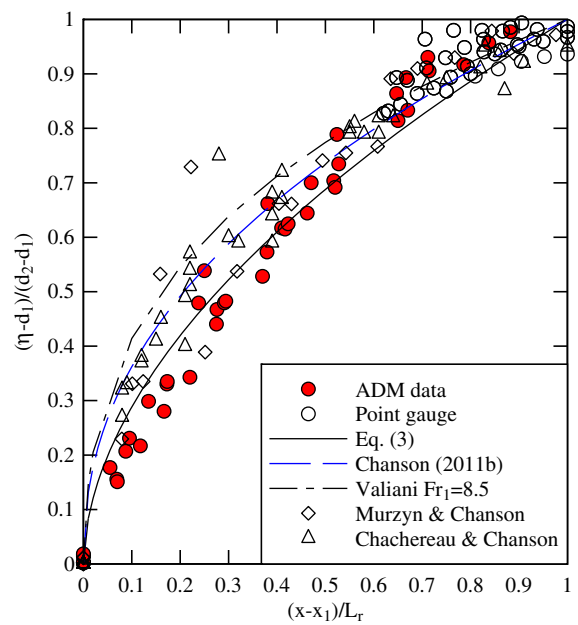

Fig. 2. Self-similar free-surface profiles within the roller length: comparison between experimental data from the present study, Murzyn and Chanson (2009), Chachereau and Chanson (2011); Eq. (3); and the correlations of Valiani (1997) and Chanson (2011b)

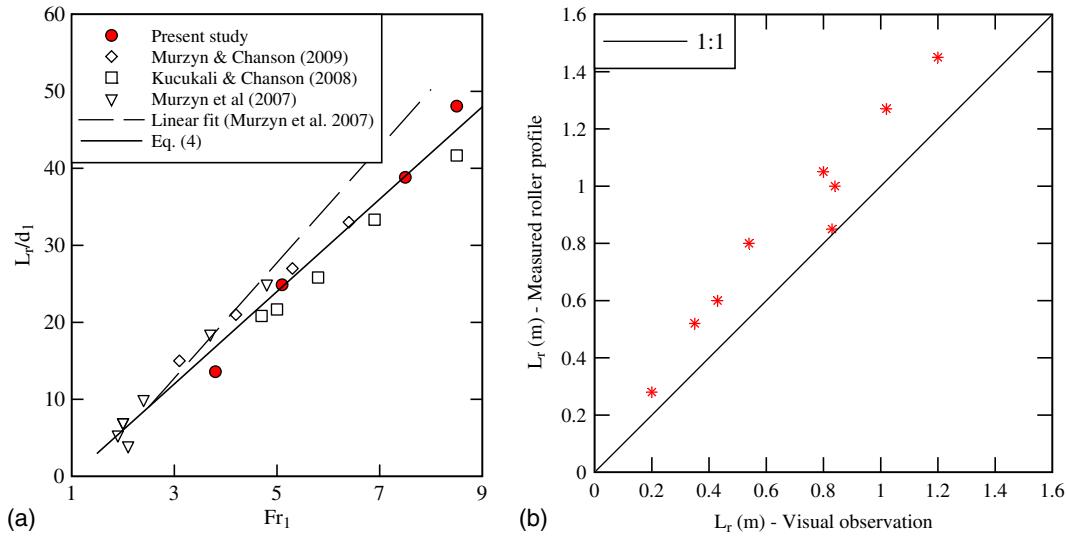

Fig. 3. Hydraulic jump roller length: (a) dimensionless roller length as a function of the Froude number: comparison with experimental data from Murzyn et al. (2007), Kucukali and Chanson (2008), Murzyn and Chanson (2009); the correlation of Murzyn et al. (2007); and Eq. (4); (b) comparison between roller length data: visual observations versus profile measurements

frequency of approximately 0.004 Hz, with longitudinal deviation of up to half the roller length (Fig. 4). Although such slow and large fluctuations in hydraulic jump positions were documented for oscillating jumps (Mossa 1999), the present findings provided quantitative evidences of the phenomenon with breaking hydraulic jumps for $3.8 < F_1 < 8.5$.

The fast fluctuations of jump toe position were documented in earlier studies (Long et al. 1991; Chanson and Gualtieri 2008). It is believed that the rapid jump toe oscillation is related to the air entrapment at the impingement point, generation of large turbulent structures, and their advection in the developing shear layer, including vortex pairing (Long et al. 1991). In this paper, the longitudinal jump toe oscillations were detected from upstream

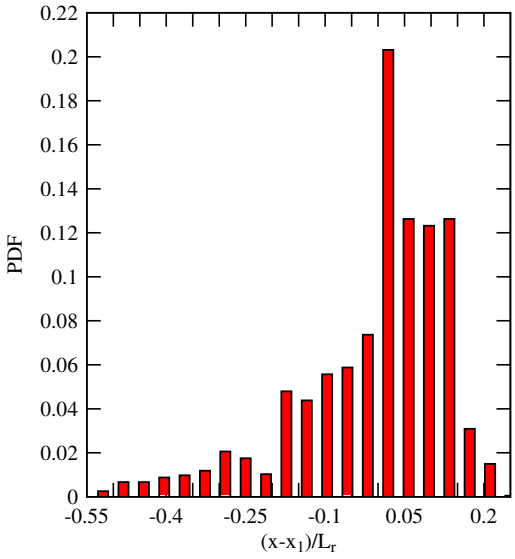

Fig. 4. Probability density function distribution of instantaneous jump toe position: slow fluctuations (recording time: 160 min) with flow conditions of $Q = 0.0239$ m^3/s, $d_1 = 0.0209$ m, $x_1 = 0.83$ m, $F_1 = 5.1$, and $R = 4.8 \times 10^4$

using horizontally mounted acoustic displacement meters (Fig. 5). A sketch of the experimental setup is shown in Figs. 5(a and b), and the results are presented in Figs. 5(c and d). The characteristic oscillation frequencies were deduced from a spectral analysis of the displacement meter signals. The data showed both dominant and secondary frequencies, denoted $F_{toe,dom}$ and $F_{toe,sec}$, respectively. Typical results are shown in Figs. 5(c and d) as functions of the inflow Froude number and Reynolds number, respectively, and compared with previous visual observations of jump toe oscillation frequencies [same legend for Figs. 5(c and d)]. The present data encompassed those with a constant Froude number ($F_1 = 5.1$) for different Reynolds numbers, as well as the data with a constant gate opening ($h = 0.020$ m) for $F_1 = 3.8$, 5.1, 7.5, and 8.5.

The experimental data yielded characteristic Strouhal numbers $S = F_{toe,dom} \times d_1/V_1$ in a range of 0.005–0.015, and the results were basically independent of the sensor's transverse location. Some dimensionless secondary frequencies were also observed, with Strouhal numbers $S = F_{toe,sec} \times d_1/V_1$ typically higher than 0.02. Both present and earlier data were close, except for the data of Zhang et al. (2013) and Chachereau and Chanson (2011) at low Froude numbers ($F_1 < 4.4$). In these two studies, higher frequencies were observed at Froude numbers less than 4.4 with an exponential decay in dimensionless frequency with increasing Froude number [Fig. 5(c)]. Fig. 5(d) presents also the results as functions of the Reynolds number between 2.1×10^4 and 1.63×10^5. Higher dominant frequencies were seen at larger Reynolds numbers, whereas no apparent effect of the Reynolds number is shown in terms of the secondary frequencies. The secondary frequencies were thought to be linked to the vertical free-surface fluctuations above the roller, as they were shown in a same frequency range.

The amplitudes of fast fluctuations of jump toe oscillations were characterized with the standard deviations of instantaneous jump front position x'. The results on the channel centerline are presented in Fig. 6 as a function of the inflow Froude number. The toe oscillation amplitude increased with increasing Froude number and the present data were best correlated by

$$\frac{X'}{d_1} = 0.11 \times F_1 + 0.5 \quad 3.8 < F_1 < 8.5 \tag{5}$$

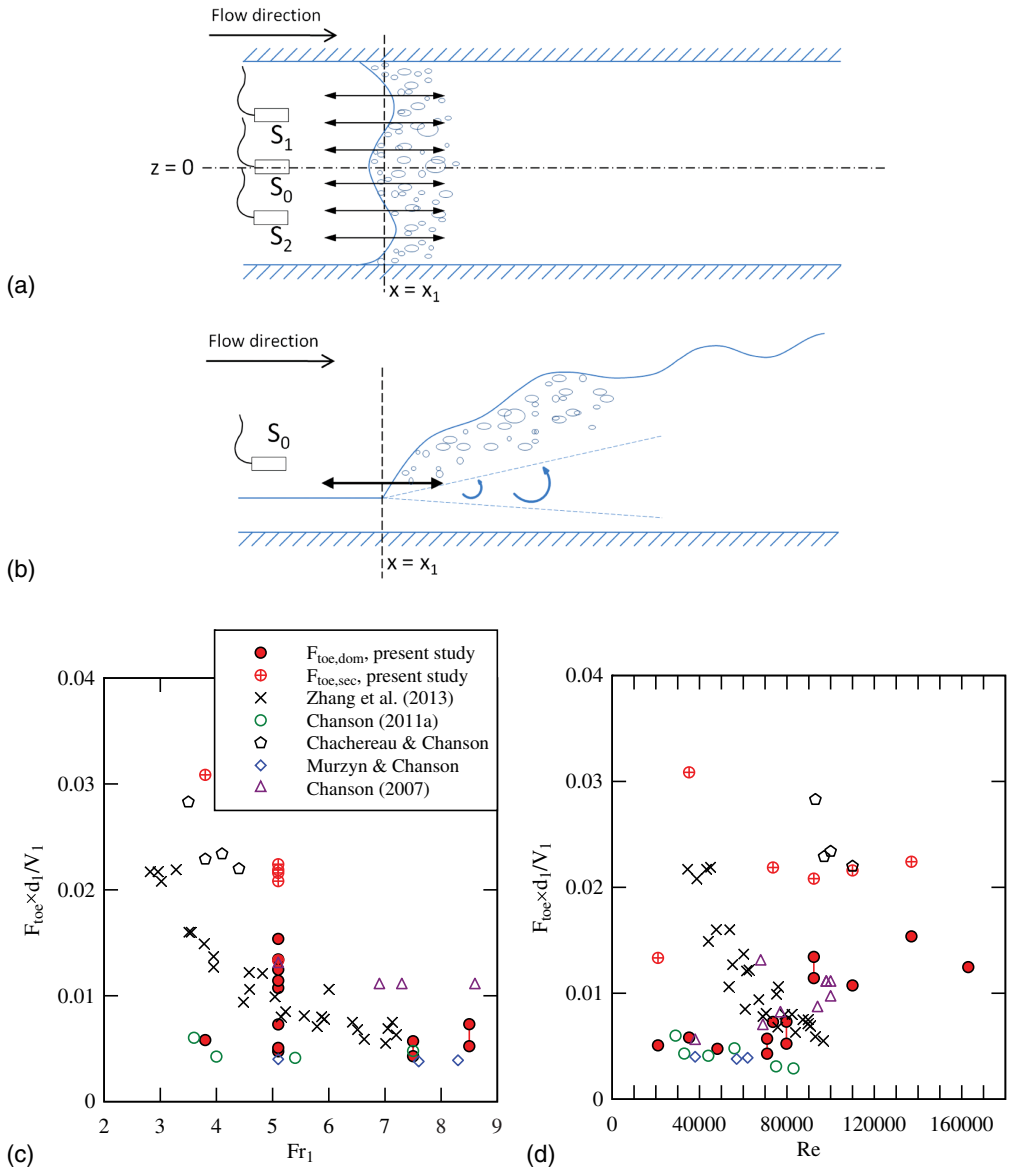

Fig. 5. Measurements of rapid fluctuations of longitudinal jump toe positions using acoustic displacement meters: (a) sketch of longitudinal jump toe oscillation measurements: top view; (b) sketch of longitudinal jump toe oscillation measurements: side view; (c and d) dimensionless characteristic frequencies of jump toe oscillation on the channel centerline as functions of the inflow Froude number (c) and the Reynolds number (d) in comparison with the visual observation results of Chanson (2007), Murzyn and Chanson (2009), Chanson (2011a), Chachereau and Chanson (2011), and Zhang et al. (2013)

Eq. (5) is compared with the data in Fig. 6 and the earlier data of Long et al. (1991). The results were independent of the Reynolds number. Moreover, larger transverse coherent structures were observed in the wavelike impingement perimeter for stronger hydraulic jumps, as first reported by Zhang et al. (2013). The present observations showed stronger correlations between the signals of two transversely separated displacement meters for higher Froude and Reynolds numbers and sketched in Fig. 5.

Two-Phase Flow Properties in the Roller

The experimental observations demonstrated the intense aeration of the jump roller. The air–water flow properties of hydraulic jumps were studied systematically. Typical vertical distributions of time-averaged void fraction are presented in Fig. 7(a). The void fraction data showed two distinct flow regions, namely, the shear layer between the channel bed and an elevation y^* of local minimum void fraction, and the upper free-surface region above, in which the void fraction increased monotonically with distance from the invert [Fig. 7(a)]. The shear layer was characterized by the advection of highly aerated large vortical structures generated at the impingement point, and the void fraction distribution showed a local maximum C_{max}. The void fraction profile followed closely an analytical solution of two-dimensional diffusion equation for air bubbles (Crank 1956)

$$V_1 \times \frac{\partial C}{\partial x} = D_t \times \frac{\partial^2 C}{\partial y^2} \tag{6}$$

where D_t = air bubble diffusivity in the shear layer; C = time-averaged void fraction; and y = vertical elevation. Assuming a

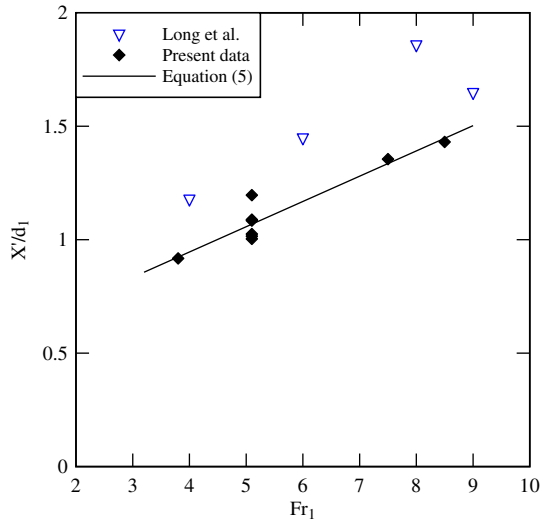

Fig. 6. Standard deviation x' of the horizontal jump toe location as function of the inflow Froude number; data collected with acoustic displacement sensors mounted horizontally; comparison with Eq. (5) and the data of Long et al. (1991)

uniform velocity field, constant diffusivity, and neglecting the compressibility effects, a simplified solution of Eq. (6) is

$$C = C_{max} \times \exp\left[-\frac{1}{4 \times D^{\#}} \times \frac{\left(\frac{y-y_{Cmax}}{d_1}\right)^2}{\left(\frac{x-x_1}{d_1}\right)^2}\right] \quad \text{Shear layer} \qquad (7)$$

where $D^{\#} = D_t/(V_1 \times d_1)$; and y_{Cmax} = distance from the bed where $C = C_{max}$ (Chanson 1995, 2011a). Eq. (7) is compared with some data in Fig. 7(a) at different longitudinal locations in a hydraulic jump. The results showed the broadening of the two-phase shear region, and the maximum void fraction C_{max} in the shear layer was observed to decrease exponentially with increasing distance from the jump toe. Further, the location y_{Cmax} of the local maximum in void fraction was seen to increase linearly with increasing distance from the impingement. The present data showed some dependence upon the Froude number, and they were best correlated by

$$C_{max} = 0.40 \times \exp\left[-\frac{1}{2 \times (F_1 - 1)} \times \frac{x - x_1}{d_1}\right] \quad 3.8 < F_1 < 8.5 \qquad (8)$$

$$\frac{y_{Cmax}}{d_1} = 1.479 + 0.084 \times \frac{x - x_1}{d_1} \quad 3.8 < F_1 < 8.5 \qquad (9)$$

In the upper free-surface region, the void fraction distribution may be approximated by a Gaussian error function

$$C = \frac{1}{2} \times \left\{1 + erf\left[\frac{y - y_{50}}{2 \times (x - x_1) \times \sqrt{D^*}}\right]\right\} \quad \text{Upper free-surface} \qquad (10)$$

where y_{50} = characteristic elevation where $C = 0.50$; and D^* = dimensionless diffusivity in the free-surface region. Eq. (10) is shown with dashed lines in Fig. 7(a).

The bubble count rate is defined as the number of bubbles detected per second. Independently of the bubble shape and size distribution, the bubble count rate is proportional to the air–water interface area, hence, to the re-aeration rate. Typical vertical distributions are shown in Fig. 7(b) for the same flow conditions as the data presented in Fig. 7(a). The data indicated a marked maximum F_{max} in bubble count rate located in the air–water shear region: i.e., $1 < y_{Fmax}/d_1 < 2$ in Fig. 7(b). This maximum bubble count rate was linked to the region of maximum shear stress. For $y > y_{Fmax}$, the bubble count rate decreased with increasing elevation. The present data showed some dependence upon the flow conditions, and they were best correlated by

$$\frac{F_{max} \times d_1}{V_1} = (0.343 + 0.131 \times 10^{-4} \times R) \times \exp\left[-\frac{1}{2.67 \times (F_1 - 1)} \times \frac{x - x_1}{d_1}\right] \quad 3.8 < F_1 < 8.5 \qquad (11)$$

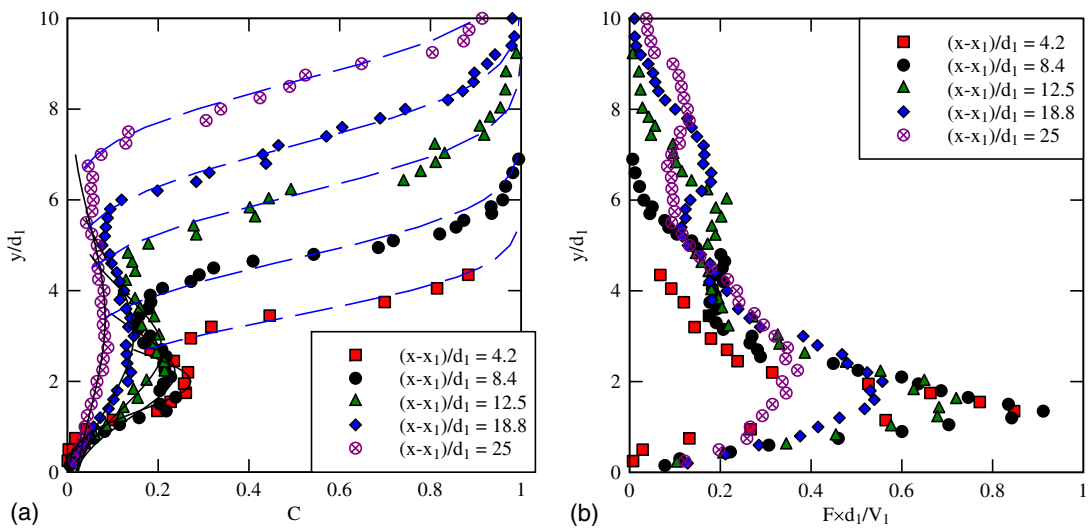

Fig. 7. Vertical distributions of void fraction C and bubble count rate F at several longitudinal cross sections in the hydraulic jump roller with flow conditions $Q = 0.0397$ m^3/s, $d_1 = 0.020$ m, $x_1 = 0.83$ m, $F_1 = 8.5$, and $R = 8.0 \times 10^4$: (a) void fraction data: comparison with Eq. (7) (solid lines) and Eq. (10) (dashed lines); (b) bubble count rate data

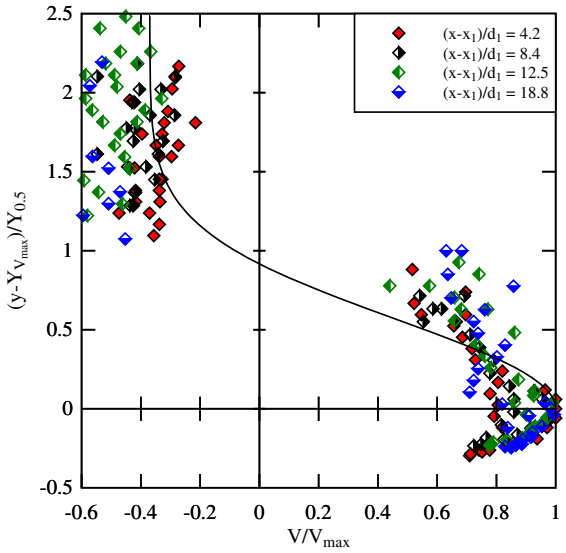

Fig. 8. Vertical distributions of time-averaged interfacial velocity V in the hydraulic jump roller with flow conditions $Q = 0.0333$ m^3/s, $d_1 = 0.020$ m, $x_1 = 0.83$ m, $\mathsf{F}_1 = 7.5$, and $\mathsf{R} = 6.6 \times 10^4$ in comparison with Eq. (13)

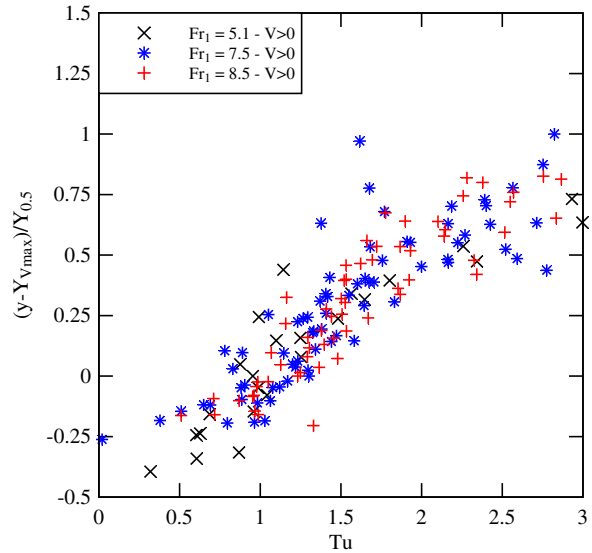

Fig. 9. Vertical distributions of turbulence intensity Tu in the hydraulic jump roller with flow conditions $Q = 0.0333$ m^3/s, $d_1 = 0.020$ m, $x_1 = 0.83$ m; data set corresponding to $V > 0$ only

$$\frac{y_{F\max}}{d_1} = 1.2 + 0.045 \times \frac{x - x_1}{d_1} \quad 3.8 < \mathsf{F}_1 < 8.5 \qquad (12)$$

The vertical distributions of time-averaged longitudinal velocity V were recorded using a Pitot tube in the clear-water flow region and the dual-tip phase detection probe in the aerated flow region based upon a cross-correlation analysis. Some typical data are shown in Fig. 8. Overall the longitudinal velocity data exhibited vertical profiles similar to those for a wall jet (Rajaratnam 1965; Chanson and Brattberg 2000)

$$\frac{V}{V_{\max}} = \left(\frac{y}{Y_{V\max}}\right)^{1/N} \quad \text{for } y/y_{V\max} < 1 \qquad (13a)$$

$$\frac{V - V_{\text{recirc}}}{V_{\max} - V_{\text{recirc}}} = \exp\left[-\frac{1}{2} \times \left(1.765 \times \frac{y - Y_{V\max}}{Y_{0.5}}\right)^2\right] \quad \text{for } y/Y_{V\max} > 1 \qquad (13b)$$

where $V_{\max}$ = maximum velocity in the shear layer and $Y_{V\max}$ = corresponding elevation; N = constant; V_{recirc} = (negative) recirculation velocity in the upper free-surface region; and $Y_{0.5}$ = elevation, where $V = V_{\max}/2$. The recirculation velocity V_{recirc} was found nearly uniform at a given longitudinal position across the recirculation region, whereas $N = 6$ to 10 typically. In the region where the interfacial velocity was about zero, some analysis of instantaneous time lag in the raw probe signals supported the continuous velocity profile prediction by showing small average velocity close to $y(V = 0)$ (see "Discussion").

The turbulence intensity was derived from the cross-correlation analysis of dual-tip probe signals, following Kipphan (1977) for two-phase gas-solid mixtures and Chanson and Toombes (2002) in high-velocity free-surface flows. Typical results are presented in Fig. 9 in which the data are shown for positive velocity measurements only. In the shear region, the turbulence intensity increased with increasing vertical elevation y and with increasing Froude number. The former trend would be consistent with the Prandtl mixing length theory for a wall jet as well as monophase hydraulic jump data (Rouse et al. 1959; Liu et al. 2004).

Discussion on the Validity of Turbulence Measurements

The present results showed unusually large turbulence levels in the hydraulic jump roller, as previously reported by Murzyn and Chanson (2009) and Chanson (2011b) and by using a similar metrology. It is believed that the large turbulence intensity levels were linked to a combination of roller position oscillations and singularity of the probe correlation analyses. The longitudinal oscillations of jump toe around a mean position x_1 impacted on the Eulerian phase-detection probe data. Assuming that the roller position oscillated periodically with time t

$$X(t) = x_1 + a \times \sin(2 \times \pi \times F_{\text{toe}} \times t) \qquad (14)$$

the roller motion induced a quasi-periodic oscillation of the longitudinal velocity component with a similar frequency F_{toe}. The instantaneous interfacial velocity $V(t)$ could be expressed as the sum of a mean value, a periodic fluctuation, and a turbulent fluctuation. The turbulence intensity Tu was thus the sum of the oscillating velocity fluctuation plus true turbulent fluctuations

$$Tu = \frac{V'}{V} = \frac{\pi \times a \times F_{\text{toe}}}{V} + \frac{v'}{V} \qquad (15)$$

where V' = root mean square of the instantaneous velocity; and v' = root mean square of the turbulent fluctuation. This simple development shows that the apparent turbulent intensity Tu increases with increasing jump toe oscillation frequency and amplitude, and it becomes very significant in regions of small velocity magnitude. For $a = 0.03$ m, $F_{\text{toe}} = 1.5$ Hz, and $V = 0.5$ m/s, the dimensionless oscillating velocity fluctuation is 0.3. The preceding development implicitly assumed a horizontal translation of the roller about a mean position and did not consider a deformation of roller. Furthermore, the effects of the pseudo-periodic production of large vortices in the velocity field were implicitly neglected (Wang et al. 2014).

A limitation of the dual-tip phase-detection probe was the cross-correlation analysis, implicitly assuming a single direction of the interface advection. At the transition between shear layer

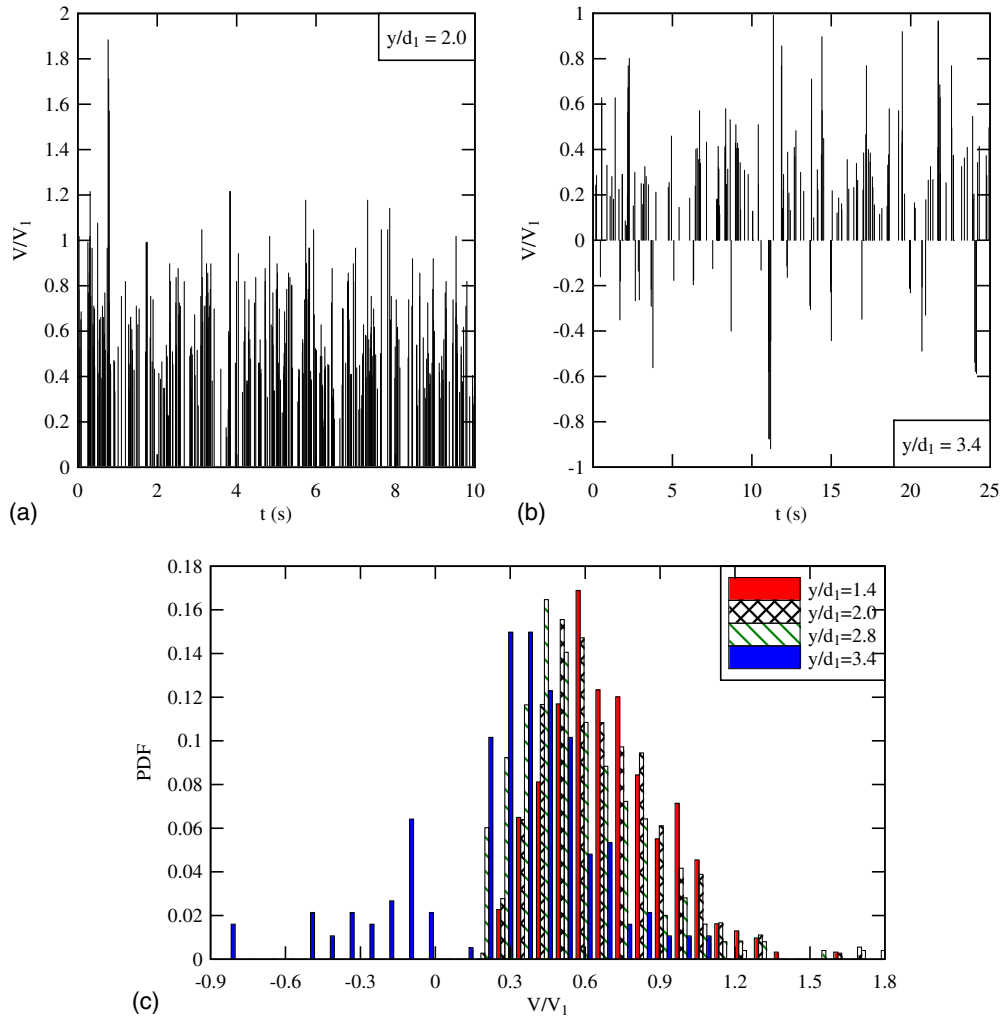

Fig. 10. Instantaneous interfacial velocity data derived from individual bubble detections in flow conditions $F_1 = 8.5$, $R = 7.5 \times 10^4$, $Q = 0.0378$ m^3/s, $d_1 = 0.020$ m, $x_1 = 0.83$ m, x-$x_1 = 0.25$ m, and $V_1 = 3.78$ m/s: (a) $y/d_1 = 2.0$; (b) $y/d_1 = 3.4$; (c) probability density function of instantaneous interfacial velocities derived from a manual analysis

and recirculation region, the instantaneous velocity switched between positive and negative values, while the average velocity was close to zero. For such flow conditions, raw probe signals were analyzed manually based upon the detection of individual bubbles to yield instantaneous interfacial velocity data (Fig. 10). Figs. 10(a and b) present typical time variations of instantaneous interfacial velocity based upon this manual processing. Fig. 10(c) compared the probability density functions (PDFs) of dimensionless velocities at several elevations. The probability density function followed a normal distribution, which typically implied a pseudo-homogeneous, stationary turbulence field in the shear layer (Batchelor 1967). A zero instantaneous velocity was difficult to distinguish because very few bubbles were advected past the probe.

The time-averaged velocity V and turbulence intensity Tu were calculated based upon the individual bubble event data sets and the results were compared with the cross-correlation analysis results, although it is acknowledged that large instantaneous velocity deviations might be ignored. The comparison showed close results in terms of the time-averaged velocity in the lower shear layer. In the upper shear layer, the manual analysis showed some instantaneous negative velocities [Fig. 10(b)], which could not be distinguished by cross-correlation processing and led to an overestimation of both interfacial velocity and turbulence intensity. On the other hand, the manually calculated turbulence intensity was consistently smaller than those deduced from cross-correlation analysis, and the differences increased drastically in the flow region, where the instantaneous velocity switched between negative and positive values.

Conclusion

The turbulent fluctuations in hydraulic jumps were investigated physically in a relatively large-size channel. Both nonintrusive acoustic displacement meters and an intrusive phase-detection probe were used. The inflow Froude number varied from 3.8 to 8.5, and the Reynolds number ranged from 2.1×10^4 to 1.63×10^5. The time-averaged free-surface profile of the jump roller presented a self-similar profile. The longitudinal movements of the jump were observed, and both fast and very slow fluctuations were documented. Long-period shifts in jump position about its mean occurred with periods up to 400 s with movements of up to half the roller length from the mean position. The fast oscillations in jump toe position were found to be around a dominant frequency with some secondary frequency.

The air–water flow measurements quantified the intense aeration of the roller. The void fraction data were closely matched by theoretical solutions of the advective diffusion equation in the shear layer and upper free-surface region. The interfacial velocity distributions presented a smooth shape close to a wall jet profile, with a negative recirculation motion in the upper flow region. Large turbulence intensities were recorded using a cross-correlation analysis. It was shown that these large values might derive from the combined effects of large longitudinal roller fluctuations and of some singularity of the metrology for $V = 0$.

The observations highlighted the role of large vortical structures, generated at the impingement point and advected in the developing shear layer. The eddies were highly aerated and three-dimensional. Overall, the present findings demonstrated the complex nature of turbulent hydraulic jumps and the close interactions between the roller turbulence and free-surface fluctuations. Future investigations should be carried out over long durations to account for the very slow fluctuations in jump position.

Acknowledgments

The authors acknowledge the generous advice of Dr. Frédéric Murzyn (ESTACA Laval, France). They thank the technical staff of the School of Civil Engineering at the University of Queensland for their assistance. The financial support of the Australian Research Council (Grant DP120100481) is acknowledged.

Notation

The following symbols are used in this paper:

a = amplitude (m) of roller toe fluctuation;
C = void fraction defined as the volume of air per unit volume of air and water;
C_{max} = local maximum in void fraction in the developing shear layer;
D_t = air bubble diffusivity (m^2/s) in the air–water shear layer;
$D^{\#}$ = dimensionless air bubble diffusivity: $D^{\#} = D_t/(V_1 \times d_1)$;
D^* = dimensionless diffusivity in the upper free-surface region;
d_1 = flow depth (m) measured immediately upstream of the hydraulic jump;
d_2 = downstream conjugate flow depth (m);
F = bubble count rate (Hz) defined as the number of bubbles impacting the probe sensor per second;
F_{max} = maximum bubble count rate (Hz) in the air–water shear layer;
F_{toe} = hydraulic jump toe oscillation frequency (Hz);
$F_{toe.dom}$ = primary hydraulic jump toe oscillation frequency (Hz);
$F_{toe.\,sec}$ = secondary hydraulic jump toe oscillation frequency (Hz);
F_1 = upstream Froude number: $\mathsf{F}_1 = V_1/\sqrt{g \times d_1}$;
g = gravity acceleration (m/s^2): $g = 9.80\ m/s^2$ in Brisbane (Australia);
L_r = roller length (m);
Q = water discharge (m^3/s);
R = Reynolds number: $\mathsf{R} = \rho \times V_1 \times d_1/\mu$;
Tu = turbulence intensity: $Tu = V'/V$;
V = time-averaged air–water velocity (m/s);
V' = root mean square of velocity fluctuations (m/s);
V_1 = upstream flow velocity (m/s): $V_1 = Q/(W \times d_1)$;
V_{max} = maximum velocity (m/s);
V_{recirc} = recirculation velocity (m/s) in the upper free-surface velocity;
v' = root mean square of turbulent velocity fluctuations (m/s);
W = channel width (m);
X = instantaneous roller toe position (m);
x' = root mean square of roller toe position (m);
x = longitudinal distance from the upstream sluice gate (m);
x_1 = longitudinal distance from the upstream gate to the jump toe (m);
$Y_{0.5}$ = vertical elevation (m) where $V = V_{max}/2$;
y = distance (m) measured normal to the flow direction;
y_{50} = characteristic distance (m) from the bed where $C = 0.50$;
y_{Cmax} = vertical elevation (m) where the void fraction in the shear layer is maximum ($C = C_{max}$);
y_{Fmax} = distance (m) from the bed where the bubble count rate is maximum ($F = F_{max}$);
Y_{Vmax} = vertical elevation (m) where the velocity is maximum ($V = V_{max}$);
Δx = longitudinal distance (m) between probe sensors;
Δz = transverse distance (m) between probe sensors;
δ = boundary layer thickness (m);
η = roller free-surface elevation (m);
μ = dynamic viscosity (Pa · s) of water;
ρ = density (kg/m^3) of water; and
Ø = diameter (m).

Subscripts

1 = initial flow conditions; and
2 = downstream conjugate flow conditions.

References

Babb, A. F., and Aus, H. C. (1981). "Measurements of air in flowing water." *J. Hydraul. Div.*, 107(HY12), 1615–1630.

Batchelor, G. K. (1967). "Brownian diffusion of particles with hydrodynamic interaction." *J. Fluid Mech.*, 74(1), 1–29.

Chachereau, Y., and Chanson, H. (2011). "Free-surface fluctuations and turbulence in hydraulic jumps." *Exp. Therm. Fluid Sci.*, 35(6), 896–909.

Chanson, H. (1995). "Air entrainment in two-dimensional turbulent shear flows with partially developed inflow conditions." *Int. J. Multiphase Flow*, 21(6), 1107–1121.

Chanson, H. (2007). "Bubbly flow structure in hydraulic jump." *Eur. J. Mech. B/Fluids*, 26(3), 367–384.

Chanson, H. (2009). "Current knowledge in hydraulic jumps and related phenomena. A survey of experimental results." *Eur. J. Mech. B/Fluids*, 28(2), 191–210.

Chanson, H. (2011a). "Bubbly two-phase flow in hydraulic jumps at large Froude numbers." *J. Hydraul. Eng.*, 10.1061/(ASCE)HY.1943-7900.0000323, 451–460.

Chanson, H. (2011b). "Hydraulic jumps: Turbulence and air bubble entrainment." *J. La Houille Blanche*, 1(3), 5–16.

Chanson, H. (2012). "Momentum considerations in hydraulic jumps and bores." *J. Irrig. Drain. Eng.*, 10.1061/(ASCE)IR.1943-4774.0000409, 382–385.

Chanson, H., and Brattberg, T. (2000). "Experimental study of the air–water shear flow in a hydraulic jump." *Int. J. Multiphase Flow*, 26(4), 583–607.

Chanson, H., and Gualtieri, C. (2008). "Similitude and scale effects of air entrainment in hydraulic jumps." *J. Hydraul. Res.*, 46(1), 35–44.

Chanson, H., and Montes, J. S. (1995). "Characteristics of undular hydraulic jumps. Experimental apparatus and flow patterns." *J. Hydraul. Eng.*, 10.1061/(ASCE)0733-9429(1995)121:2(129), 129–144.

Chanson, H., and Toombes, L. (2002). "Air–water flows down stepped chutes: Turbulence and flow structure observations." *Int. J. Multiphase Flow*, 28(11), 1737–1761.

Crank, J. (1956). *The mathematics of diffusion*, Oxford University Press, London.

Hager, W. H. (1992). *Energy dissipators and hydraulic jump*, Vol. 8, Water Science and Technology Library, Kluwer Academic, Dordrecht, Netherlands, 288.

Henderson, F. M. (1966). *Open channel flow*, MacMillan, New York.

Kipphan, H. (1977). "Bestimmung von Transportkenngrößen bei Mehrphasenströmungen mit Hilfe der Korrelationsmeßtechnik." *Chemie Ingenieur Technik*, 49(9), 695–707 (in German).

Kucukali, S., and Chanson, H. (2008). "Turbulence measurements in hydraulic jumps with partially-developed inflow conditions." *Exp. Therm. Fluid Sci.*, 33(1), 41–53.

Lennon, J. M., and Hill, D. F. (2006). "Particle image velocimetry measurements of undular and hydraulic jumps." *J. Hydraul. Eng.*, 10.1061/(ASCE)0733-9429(2006)132:12(1283), 1283–1294.

Liggett, J. A. (1994). *Fluid mechanics*, McGraw-Hill, New York.

Liu, M., Rajaratnam, N., and Zhu, D. Z. (2004). "Turbulent structure of hydraulic jumps of low Froude numbers." *J. Hydraul. Eng.*, 10.1061/(ASCE)0733-9429(2004)130:6(511), 511–520.

Long, D., Rajaratnam, N., Steffler, P. M., and Smy, P. R. (1991). "Structure of flow in hydraulic jumps." *J. Hydraul. Res.*, 29(2), 207–218.

Mossa, M. (1999). "On the oscillating characteristics of hydraulic jumps." *J. Hydraul. Res.*, 37(4), 541–558.

Murzyn, F., and Chanson, H. (2009). "Free-surface fluctuations in hydraulic jumps: Experimental observations." *Exp. Therm. Fluid Sci.*, 33(7), 1055–1064.

Murzyn, F., Mouaze, D., and Chaplin, J. R. (2007). "Air–water interface dynamic and free surface features in hydraulic jumps." *J. Hydraul. Res.*, 45(5), 679–685.

Ohtsu, I., Yasuda, Y., and Gotoh, H. (2001). "Hydraulic condition for undular-jump formations." *J. Hydraul. Res.*, 39(2), 203–209.

Rajaratnam, N. (1965). "The hydraulic jump as a wall jet." *J. Hydraul. Div.*, 91(HY5), 107–132.

Rajaratnam, N. (1967). "Hydraulic jumps." *Advances in hydroscience*, Vol. 4, V. T. Chow, ed., Academic, New York, 197–280.

Resch, F. J., Leutheusser, H. J., and Alemu, S. (1974). "Bubbly two-phase flow in hydraulic jump." *J. Hydraul. Div.*, 100(HY1), 137–149.

Rouse, H., Siao, T. T., and Nagaratnam, S. (1959). "Turbulence characteristics of the hydraulic jump." *Transactions*, 124, 926–950.

Valiani, A. (1997). "Linear and angular momentum conservation in hydraulic jump." *J. Hydraul. Res.*, 35(3), 323–354.

Vallé, B. L., and Pasternack, G. B. (2006). "Air concentrations of submerged and unsubmerged hydraulic jumps in a bedrock step-pool channel." *J. Geophys. Res.*, 111(F3), 12.

Wang, H., and Chanson, H. (2013). "Free-surface deformation and two-phase flow measurements in hydraulic jumps." *Hydraulic Model Rep. No. CH91/13*, School of Civil Engineering, Univ. of Queensland, Brisbane, Australia, 108.

Wang, H., Felder, S., and Chanson, H. (2014). "An experimental study of turbulent two-phase flow in hydraulic jumps and application of a triple decomposition technique." *Exp. Fluids*, 55(7), 18.

Zhang, G., Wang, H., and Chanson, H. (2013). "Turbulence and aeration in hydraulic jumps: Free-surface fluctuation and integral turbulent scale measurements." *Environ. Fluid Mech.*, 13(2), 189–204.